High-Efficiency Solution-Processed Two-Terminal Hybrid Tandem Solar Cells Using Spectrally Matched Inorganic and Organic Photoactive Materials

Havid Aqoma, Imil Fadli Imran, Febrian Tri Adhi Wibowo, Narra Vamsi Krishna, Wooseop Lee, Muhammad Shamim Al Mamun, Du Yeol Ryu, Sung-Yeon Jang*

Dr. H. Aqoma, I. F. Imran, F. T. A. Wibowo, Dr. N. V. Krishna, Prof. S.-Y. Jang
School of Energy and Chemical Engineering, Ulsan National Institute of Science and Technology (UNIST), 50 UNIST-gil, Ulsan 44919, Republic of Korea.
E-mail: syjang@unist.ac.kr
W. Lee, D. Y. Ryu
Department of Chemical and Biomolecular Engineering, Yonsei University, 50 Yonsei-ro, Seodaemun-gu, Seoul 03722, Republic of Korea
M. S. A. Mamun
Department of Chemistry, Kookmin University, 77 Jeongneung-ro, Seongbuk-gu, Seoul 02707, Republic of Korea

Although the power conversion efficiency (PCE) of inorganic perovskite-based solar cells (PSCs) has been considerably less than that of organic-inorganic hybrid PSCs due to their wider bandgap, inorganic perovskites are great candidates for the front cell in tandem devices. Herein, we demonstrate the great potential of low-temperature solution-processed two-terminal hybrid tandem solar cell devices based on spectrally matched inorganic perovskite and organic bulk heterojunction for the front and back cells, respectively. By matching optical properties of front and back cells in the hybrid tandem device by using $CsPbI_2Br$ and PTB7-Th:IEICO-4F BHJ as the active materials, we achieved a remarkably enhanced PCE in the hybrid tandem (18.04%) as compared to that of the single-junction device (12.46% for $CsPbI_2Br$ and 11.02% for PTB7-Th:IEICO-4F). Notably, the PCE of our hybrid tandem device is thus far the highest PCE among the reported tandem devices based on perovskite and organic material. Moreover, the long-term stability of inorganic perovskite devices under stress of humidity was improved in the hybrid tandem device due to the hydrophobicity of the PTB7-Th:IEICO-4F back cell. In addition, the potential promise of this type of hybrid tandem device was calculated, where a PCE of as much as

~28% is possible by improving the external quantum efficiency and reducing energy loss in the sub-cells.

1. Introduction

Perovskite solar cells (PSCs) have attracted considerable interest over the past decades due to their marvelous optical and electrical properties, such as low exciton binding energy,[1] high absorption coefficient,[2] long charge diffusion length,[3] and low trap-state density.[4] Intensive research in organic-inorganic hybrid perovskite (OIHP)-based solar cells has increased the power conversion efficiency (PCE) rapidly from 3.8% to 25.2%.[5] However, the state-of-the-art OIHP-based PSCs contain volatile organic components (such as the methylammonium ($CH_3NH_3^+$) and formamidinium ($CHN_2H_4^+$) groups), which is the origin of phase instability under thermal, moisture, and oxygen stresses.[6, 7] By contrast, all-inorganic perovskites have also emerged as excellent alternative materials with enhanced thermal stability.[8] However, the PCE of inorganic perovskite-based device is considerably less than that of OIHP-based PSCs,[9] whereas their cubic phase remains unstable and transforms to the yellow δ phase under humidity stress.[10]

In previous studies, inorganic $CsPbBr_3$ perovskite showed sufficient phase stability at room temperature (RT). However, a too-wide bandgap (~2.30 eV) has been unfavorable for a photoactive material in PSCs.[11, 12] The cubic $CsPbI_3$ has a more suitable bandgap (~1.73 eV). Nevertheless, the black cubic phase is stable only at a high temperature (>320 °C) and rapidly converts to the orthorhombic phase with a bandgap of ~2.82 eV at RT under ambient conditions.[13, 14] By contrast, the mixed-halide-based inorganic perovskite, $CsPbI_2Br$, has demonstrated an optimal balance between the bandgap and phase stability with a PCE of 16.37% for the best-reported device.[15] The $CsPbI_2Br$ perovskite shows an intermediate bandgap of the two (~1.85 eV), whereas its cubic phase is more stable as compared to $CsPbI_3$ at RT.[16] Various attempts to improve

2

the quality of $CsPbI_2Br$ have been reported through optimization of deposition methods,[10] incorporation of additives,[17] and hydrophobic capping.[18]

Construction of tandem-structured solar cell devices can improve the PCE of single-junction cells when photon absorption is enhanced and thermalization loss is reduced.[19] Inorganic perovskites are ideal candidates for front cell in tandem devices owing to their wide bandgap (WBG) and low energy loss.[20] By contrast, organic bulk heterojunction (BHJ)-based solar cells are known to possess excellent near-infrared (NIR) absorption (down to a bandgap of ~1.25 eV).[21] In particular, the common nonpolar solvents used in the BHJ fabrication process, such as chlorobenzene or chloroform, do not damage the underlying inorganic perovskite layer. Thus, a combination of WBG inorganic perovskite as a front cell and the NIR-absorbing narrow-bandgap organic BHJ as a back cell is an excellent strategy for constructing efficient tandem solar cell devices. However, hybrid tandem devices that utilize inorganic perovskite and organic BHJ have not been investigated intensively. Thus far, the best two-terminal (2T) tandem device based on perovskite and organic BHJ has demonstrated a PCE of only 15.04%,[22, 23], which remains far below the performance of any single-junction device.

In this study, a solution-processed 2T hybrid tandem device with a PCE of 18.04% was developed by featuring $CsPbI_2Br$ inorganic perovskite and organic BHJ as front and back cells, respectively. The organic BHJ active layer consists of a mid-bandgap polymer donor, poly[4,8-bis(5-(2-ethylhexyl)thiophen-2-yl)benzo[1,2-b;4,5-b']dithiophene-2,6-diyl-alt-(4-(2-ethylhexyl)-3-fluorothieno[3,4-b]thiophene-)-2-carboxylate-2-6-diyl)] (PTB7-Th) and a low-bandgap small molecule acceptor 2,2'-((2Z,2'Z)-(((4,4,9,9-tetrakis(4-hexylphenyl)-4,9-dihydro-sindaceno[1,2-b:5,6-b']dithiophene-2,7-diyl)bis(4-((2-ethylhexyl)oxy)thiophene-5,2-diyl))bis (methanylylidene))bis(5,6-difluoro-3-oxo-2,3-dihydro-1H-indene-2,1-diylidene))dimalononitrile

(IEICO-4F). A CsPbI$_2$Br inorganic perovskite with a bandgap of ~1.85 eV and an organic BHJ with a bandgap of ~1.25 eV was chosen as a spectrally well-matched combination for 2T tandem devices based on the semi-empirical calculation. As a result, the PCE of the hybrid tandem device (~18.04%) was remarkably higher (~45%) than that of individual single-junction cells (12.46% for the CsPbI$_2$Br and 11.02% for the organic BHJ devices). Notably, this is the highest PCE reported for hybrid tandem devices based on perovskite and organic active materials thus far.[22, 23] The hybrid tandem device developed in this study also demonstrated remarkably improved long-term stability under humidity stress as compared to the CsPbI$_2$Br single-junction device because of the hydrophobicity in the back-organic BHJ layer.

2. Results and Discussion

2.1. Semi-empirical calculation of hybrid tandem devices

In this study, organic BHJ-based on PTB7-Th:IEICO-4F was employed for the back cell of the hybrid tandem devices because of its efficient NIR photon absorbability.[21, 24] The chemical structures of PTB7-Th and IEICO-4F are shown in Figure 1a. To determine the suitable bandgap for the front cells, the performance of 2T-series tandem devices with respect to front-cell bandgap ($E_{g, FC}$) was calculated using a previously reported semi-empirical analytical method (Figure 1b, more details in experimental section).[25] To calculate the PCE of the tandem device, the bandgap of the organic back cell was 1.25 eV, and the E_{loss} was set to be 0.65 eV and 0.55 eV for the front and back cells, respectively.[8, 24] The average EQE of 75% for the front cell was used, and the *FF* of the tandem device was assumed to be 0.75.[25, 26] We also assumed that the front cell entirely absorbs the photons with higher energy than its bandgap and passes through the photons with lower energy than its bandgap to the back cell.[27] Based on these parameters, the optimized PCE of the tandem devices with a CsPbI$_3$ front cell and PTB7-Th:IEICO-4F back cell was strongly dependent on the EQE$_{BC}$ (Figure 1b). The PCE was 16.73% when the EQE$_{BC}$ was 80%, whereas it was

4

18.82% at an EQE_{BC} of 90%. By contrast, the tandem devices with a $CsPbI_2Br$ front cell and PTB7-Th:IEICO-4F back cell demonstrated marginal effects of the EQE_{BC} on their optimized PCEs. The PCE of the tandem devices was 19.19% and 18.64% when the EQE_{BC} was 80% and 70%, respectively, which was higher than that of the $CsPbI_3$ front-cell-based tandem devices. In the tandem device using the $CsPbIBr_2$-based front cell, the PCE was only 15.15% regardless of the EQE_{BC} (50–90%).

We also performed a semi-empirical calculation of tandem devices with respect to the E_{loss} of the organic back cell ($E_{loss,BC}$) and the $E_{g, FC}$ (Figure 1c). All other parameters were set similar to those in Figure 1b, whereas the EQE_{BC} was assumed to be 70%.[21] It was found that the tandem devices with the $CsPbI_2Br$ perovskite as the front cell exhibited a superior PCE to those with other inorganic perovskites under the entire assumed $E_{loss,BC}$ conditions. The $CsPbI_2Br$-based tandem device reached a PCE of 19.14% with a $E_{loss,BC}$ value of 0.50 eV, whereas the $CsPbI_3$-and $CsPbIBr_2$-based tandem devices showed significantly lower PCEs (14.83% and 15.68%, respectively) under identical conditions. Note that the PTB7-Th:IEICO-4F-based single BHJ organic solar cell achieved an E_{loss} of 0.51 eV and a PCE of 10.0% in the literature.[21] By employing the $E_{loss,BC}$ value of 0.51 eV, we could perhaps enable the $CsPbI_2Br$ perovskite-based hybrid tandem device to achieve a PCE of 18.27%.

Figure 1d shows the extinction coefficient (k) values of $CsPbI_2Br$ and PTB7-Th:IEICO-4F, which were obtained from variable-angle spectroscopic ellipsometry analysis. The $CsPbI_2Br$ showed a high k value at a high photon energy (wavelength < 630 nm), whereas the PTB7-Th:IEICO-4F showed a strong absorption at low photon energy (wavelength of 600–950 nm). The complementary absorption between the $CsPbI_2Br$ and PTB7-Th:IEICO-4F is beneficial to balance the J_{SC} between the front and back cells and in turn the J_{SC} of the hybrid tandem device.

2.2. Single-junction devices

Single-junction devices using the $CsPbI_2Br$ perovskite or PTB7-Th:IEICO-4F BHJ as the active layers were first fabricated to determine proper fabrication conditions for hybrid tandem devices. The device architectures of single cells are shown in Figure S1. The $CsPbI_2Br$ active layer was prepared following the previously reported two-step thermal annealing method with slight modification.[8] The single-junction PTB7-Th:IEICO-4F device was fabricated following a reported method (Figure S1b).[24] The $J–V$ curves of optimized single-junction devices under AM 1.5G one sun illumination are shown in Figure 1e, and the device parameters are summarized in Table 1. The $CsPbI_2Br$ perovskite device yielded the best PCE of 12.46% with an active layer thickness of 400 nm (with V_{OC}, J_{SC}, and FF of 1.15 V, 13.94 mA/cm^2, and 0.78, respectively), which is comparable to those reported previously.[8] The optimized PTB7-Th:IEICO-4F single-junction device demonstrated a PCE of 11.02% at the optimum active layer thickness of 130 nm (with V_{OC}, J_{SC}, and FF of 0.70 V, 24.07 mA/cm^2, and 0.66, respectively), which is also comparable to that reported previously.[24]

Figure 1f exhibits the EQE spectra of the two single-junction devices. Based on the EQE spectra, the estimated J_{SC} of the $CsPbI_2Br$ device was 13.33 mA/cm^2 with the edge at ~650 nm, whereas that of the PTB7-Th:IEICO-4F device was 23.40 mA/cm^2 with the edge at ~970 nm. The EQE spectra of the two single-junction devices were well-separated, which indicates the efficient use of photons from solar flux at each sub-cell. The estimated J_{SC} values from the integration of EQE spectra showed a mismatch of only <3% with the measured J_{SC} in the $J-V$ curves, which confirms the reliability of our $J–V$ measurements.

2.3. Optical simulation of hybrid tandem devices

Optical simulation of the hybrid tandem devices was conducted using the transfer matrix formalism (TMF) method to elucidate the optimal thickness for the $CsPbI_2Br$ front and PTB7-Th:IEICO-4F back cells (Figure 2a). For the simulation, the refractive index (n) and k of $CsPbI_2Br$ and PTB7-Th:IEICO-4F from variable-angle spectroscopic ellipsometry analysis were used (Figure 1 and Figure S2). The simulated and measured reflectance from the hybrid tandem device with $CsPbI_2Br$ (thickness of 400 nm) and PTB7-Th:IEICO-4F (thickness of 130 nm) nearly overlapped (Figure S3), verifying the validity of the TMF optical simulation.[28] The internal quantum efficiency (IQE) of each sub-cell was obtained using a previously reported method.[29] The optical simulation revealed that the ideal thicknesses for $CsPbI_2Br$ and PTB7-Th:IEICO-4F was 350–450 nm and 80–130 nm, respectively (Figure 2a). The maximum achievable J_{SC} of the hybrid tandem device using those thicknesses was ~12.34 mA/cm^2. Notably, the J_{SC} of the hybrid tandem devices was relatively insensitive to the thicknesses of sub-cells as compared to other reported tandem devices.[25, 30, 31] This thickness insensitivity in the hybrid tandem devices derived from the fact that the optical absorption of the two sub-cells ($CsPbI_2Br$ and PTB7-Th:IEICO-4F) were nearly complementary for covering the entire visible-NIR regime (Figure 1f). Figure 2b shows the simulated absorbance of $CsPbI_2Br$ and PTB7-Th:IEICO-4F at the optimal thickness of the sub-cells. A preferential distribution in the photon absorption at the front and back cells, which cover the visible to the NIR region, was observed. This near-ideal optical property led to a near-optimal balance in the J_{SC} between two sub-cells.

Optical modeling of the normalized electric field ($|E|^2$) was investigated to elucidate the absorbed photon distribution in hybrid tandem devices (Figure 2c). The $|E|^2$ from the photons at < ~650 nm (i.e., the absorption edge of $CsPbI_2Br$) was concentrated near the ZnO/$CsPbI_2Br$ interface, whereas practically no electric field for these photons was observed in the back PTB7-Th:IEICO-4F layer.

This result indicated the complete absorption of high-energy photons (< 650 nm) at the front CsPbI$_2$Br cell. For the electric field from the photons > ~650 nm, the intensity was distributed throughout the entire hybrid tandem device, which enabled absorption in the back PTB7-Th:IEICO-4F layer. Figure 2d demonstrates the distribution of the simulated charge generation rate (G) in the hybrid tandem devices with respect to wavelengths. Because of the high k value of the CsPbI$_2$Br layer at < 650 nm (Figure 1d), the G was most populated near the ZnO/CsPbI$_2$Br interface, which indicated the minor effects from the reflected photons by the back metal electrode (Figure S4a). This result confirmed a great benefit of using CsPbI$_2$Br with a high k value as the front cell for the hybrid tandem device. By contrast, the G from the photons at >650 nm was distributed throughout the PTB7-Th:IEICO-4F back cell. Therefore, due to the back-reflected photons by the metal electrode, the thickness of ~100 nm was adequate to absorb sufficient NIR photons by the PTB7-Th:IEICO-4F layer (Figure S4b).

2.4. Hybrid tandem devices

Following the guidance from the optical simulation, we fabricated hybrid tandem devices, the architecture for which is shown in Figure 3a. An energy diagram of the hybrid tandem devices is shown in Figure 3c. For the intermediate recombination layer (IRL), the structure of the hole transport material (HTM)/Au/ETL was employed.[32] The P3HT/MoOx was used as the HTM for the CsPbI$_2$Br front cell, ZnO nanoparticles (ZnO-np) were used as the ETL for the back cell, and a thin Au layer was sandwiched between the two. We also tested another ETL for back cells, namely, poly [(9,9-bis(3'-(N,N-dimethylamino)propyl)-2,7-fluorene)-alt-2,7-(9,9–dioctylfluorene)] (PFN), which demonstrated a lower V_{OC} and FF compared to the ZnO-np-based IRL (Figure S5). We also investigated the effects of the thicknesses of front and back cells on the PCEs of tandem devices (Figures S6 and S7). Although the PCE was relatively insensitive to the

8

thicknesses, it was optimized for the front- and back-cell thicknesses of ~400 nm and ~130 nm, respectively, which was also consistent with the TMF optical modeling results (Figure 2a). The thicknesses of the sub-cells were confirmed by cross-sectional scanning electron microscopy (SEM) images (Figure 3b). The J–V curve of the hybrid tandem device under AM 1.5G one sun illumination is shown in Figure 3d, and the results are summarized in Figure 3e and Table 1. The optimized hybrid tandem device achieved a PCE of 18.04% (V_{OC} = 1.73, J_{SC} = 12.94 mA/cm^2, FF = 0.81). Figure S8 shows the stabilized maximum power output of the hybrid tandem device, which demonstrated a nearly identical PCE with that obtained from the J–V curve. The V_{OC} of the hybrid tandem device was nearly the sum of the V_{OC} in single-junction cells with a ~5% loss. The FF of the tandem device was 0.81, which was substantially higher than that of the PTB7-Th:IEICO-4F single-junction device (0.66). This high FF indicated efficient recombination of holes from the CsPbI$_2$Br front cell and electrons from the PTB7-Th:IEICO-4F back cell at the IRL.[25, 33]

It is noteworthy that the PCE of our hybrid tandem device (18.04%) was remarkably higher than that of single-junction devices (12.46% and 11.02%). The increase in PCE from a single-junction device to tandem devices was extraordinarily high (45%). In the literature, various types of tandem devices have been reported, including Si/perovskite tandem devices, which have achieved a record-high PCE (28.00%).[26, 27, 34-41] However, even in Si/perovskite- and perovskite/perovskite-based tandem devices, the improvement in PCE from single-junction to tandem devices was limited to only 15–20% (Figure 4a). In recent reports on the record-high organic/organic tandem device, only ~30% improvement in PCE from the single-junction device was achieved (13.29% to 17.50%).[25, 30, 42-49] To understand further the origins of this remarkable enhancement in our hybrid tandem device, we performed semi-empirical calculations of various tandem devices by assuming state-of-the-art parameters for the front and back cells (Figure 4b). For the calculation, the EQE$_{FC}$

and EQE_{BC} were set to be 85%, whereas the $E_{loss,FC}$ and $E_{loss,BC}$ were 0.45 eV.[38] This result revealed that our hybrid tandem device achieved near-optimal bandgap engineering for the sub-cells with ~0.95 of the calculated PCE limit.

An EQE analysis of the tandem device was conducted following a reported procedure, and the result is shown in Figure 3f.[50] Near-complementary EQE spectra from the sub-cells were observed, and the estimated J_{SC} values by the integration of front- and back-cell spectra were 13.38 and 12.57 mA/cm^2, respectively. Notably, the estimated J_{SC} values from EQE spectra were consistent with the measured J_{SC} of the hybrid tandem device from the J-V characteristic (Figure 3d). We simulated the EQE spectra of the tandem device using TMF optical modeling (solid lines in Figure 3f).[50] The simulated EQE spectra were obtained by using EQE (λ) = absorption $(\lambda,\%)$ × IQE, where the absorption value was obtained from TMF optical simulation. The IQE was obtained by combining experimental and TMF optical modeling data based on the reported procedure.[29] As Figure 3f shows, the measured and simulated EQE spectra in the hybrid tandem device were nearly identical, confirming the consistency between the experiment and simulation.

We recognized that the organic PTB7-Th:IEICO-4F back cell in the tandem device exhibited lower EQE (60–70%, Figure 3f) as compared to the EQE in the single-junction device (70–80%, Figure 1f). The lower EQE in the back cell of the tandem device might have originated from the suboptimal ETL for the back cell. In the fabrication of the single-junction organic BHJ device, the ZnO ETL by the in-situ sol-gel method (ZnO-SG) was selected because it showed an optimal performance. However, the ZnO-SG was not applicable to the IRL for the tandem device due to its annealing process at 130 ° C. To confirm the effects of ZnO-np on the performance of the organic back cell, we fabricated the single-junction organic BHJ device using ZnO-np. As Figure S9 shows, the organic BHJ single-cell using RT-processable ZnO-np showed a PCE of 9.36% with

FF of 0.60, whereas that using ZnO-SG demonstrated a PCE of 11.02% with FF of 0.66. The results are summarized in Table S1.

2.5. Long-term stability

The inorganic $CsPbI_2Br$ perovskite is known to have instability in its cubic phase against humidity stress and changes to a wider bandgap yellow phase.[10] We investigated the effect of the organic BHJ back cell on the long-term stability of inorganic $CsPbI_2Br$ perovskite cells against atmospheric humidity (~25% relative humidity). The *J–V* curve of the single-junction $CsPbI_2Br$ device and the hybrid tandem device before and after one day of humidity stress is shown in Figures 4c and 4d. The $CsPbI_2Br$ single-junction device lost its photovoltaic effects completely presumably because of the phase transformation. However, the hybrid tandem device retained ~88% of its initial PCE after 140 h (Figure 4e) (i.e., the cubic phase was maintained because of the top hydrophobic organic cell), which prevented water penetration into the bottom inorganic perovskite layer.[18]

2.5. Promise in inorganic perovskite/organic hybrid tandem solar cells

Motivated by the remarkable improvement of PCE and moisture stability in hybrid tandem devices, we again conducted a semi-empirical analysis to determine strategies for further improvement. Figure 5a shows the calculation results of tandem device performance based on the optimization of the EQE_{BC} and $E_{g,BC}$. In this calculation, we used the parameters derived from the fabricated hybrid tandem device and an $E_{loss, BC}$ of 0.55 eV. By increasing the EQE_{BC} to >75%, we could improve the PCE of the tandem device performance to >19%. An EQE_{BC} of ~75% is used because the performance of ETL in the organic back cell might be improved to match that of ZnO-SG (Figure S9). Therefore, the development of IRLs with improved ETL is required to boost the PCE of the tandem device. We also observed that the optimal $E_{g,BC}$ was shifted to a higher bandgap

when the higher EQE_{BC} was obtained. As a result, by using the organic BHJ with an EQE_{BC} of 85%, a PCE of >20% is achievable with an $E_{g,BC}$ of 1.35 eV. Considering that organic BHJ materials with a higher bandgap are more viable options,[51] we believe the improvement in the PCE of hybrid tandem devices is highly promising.

We also calculated the PCE of tandem devices based on the $E_{loss,BC}$ and $E_{g,BC}$ because a recent report on organic BHJ single-junction device revealed an energy loss of ~0.45 eV.[52] For this calculation, a moderate EQE_{BC} (65%) was used. As shown in Figure 5b, with a reduced $E_{loss,BC}$ of ~0.45 eV, a PCE of ~20% might be possible in tandem devices when using a lower bandgap organic BHJ (~1.20 eV). Figure 5c shows the tandem device performance calculation based on the bandgaps of front and back cells. The EQE_{BC} and $E_{loss,BC}$ were fixed to the values of 65% and 0.55 eV, respectively. The highest PCE of 18.92% was obtained at the $E_{g,FC}$ and $E_{g,BC}$ of 1.81 and 1.16 eV, respectively. This optimum bandgap for both sub-cells was slightly lower as compared to $CsPbI_2Br$ and PTB7-Th:IEICO-4F. However, when the back-cell bandgap was altered to match the PTB7-Th:IEICO-4F bandgap (1.25 eV), the optimum bandgap for the front-cell was 1.86 eV, which approximated that of the $CsPbI_2Br$ perovskite. The results shown in Figure 5c confirmed that our selection of sub-cell photoactive materials was nearly optimal.

We also calculated the available PCE using the best-reported device parameters for inorganic perovskite and organic BHJ solar cells, which have significantly lower E_{loss} and higher EQE than our devices. An EQE_{FC} of 0.90 and $E_{loss,FC}$ of 0.40 eV were used for the front cell,[53, 54] and an EQE_{BC} of 0.85 and $E_{loss,BC}$ of 0.45 eV were used for the back cell.[52, 55] As Figure 5d shows, the optimalbest PCE of the tandem device was 29.44% when the $E_{g,FC}$ and $E_{g,BC}$ of the tandem device was 1.65 and 0.98 eV, respectively. However, the reported lowest bandgap for organic BHJ (~1.13 eV) demonstrated a relatively low PCE (<6%).[56] Assuming a $E_{g,BC}$ of 1.25 eV, a high PCE of

28.27% can still be achieved using the CsPbI$_2$Br (1.85 eV) front cell. This is a very promising result comparable to that of state-of-the-art perovskite/Si tandem devices.[5] According to recent studies regarding enhanced long-term storage and photostability of organic BHJ devices,[57, 58] our solution-processed hybrid tandem device consisting of inorganic perovskite and organic BHJ will be a highly competitive photovoltaic technology for industrialization in the future.

3. Conclusions

In summary, we successfully demonstrated the great potential of monolithic hybrid tandem solar cells based on inorganic perovskite and organic BHJ photoactive materials. Through semi-empirical calculation and optical simulation, the selection of materials and device fabrication conditions were first studied, and then a hybrid tandem device with nearly optimized properties was fabricated. The hybrid tandem device showed remarkably higher performance as compared to that of single-junction devices. The remarkably high PCE improvement (45%) from the single-junction device (12.46% and 11.02%) to the hybrid tandem device (18.04%) was achieved because of near-optimal absorption spectral match between the two sub-cells. Notably, the PCE of 18.04% in the hybrid tandem is thus far the highest performance among the reported tandem devices based on perovskite and organic materials. Moreover, the hybrid tandem device designed in this study demonstrated significant improvement in long-term stability under humidity stress, which is due to the hydrophobicity of the organic BHJ back-cell layer. In addition, this study rationally suggested the possibility of achieving a PCE of as much as ~28% in the inorganic perovskite/organic hybrid tandem devices by improving EQE and reducing energy loss in the sub-cells.

4. Experimental Section

Single-junction device fabrication: The ITO/glass substrate was cleaned using sonication with acetone and isopropyl alcohol for 20 min each. The solvent was dried in a vacuum oven at 100 °C

for a minimum of 2 h. Prior to the spin-coating process, the substrate was treated using UV ozone for 20 min. The single-junction $CsPbI_2Br$ device used a ZnO nanoparticles and was synthesized following the reported method.[59] The ZnO nanoparticles was spin-coated at 4000 rpm for 30 s to achieve ~20 nm thickness, and was followed by a 5-min thermal annealing process at 200 °C. The substrate was transferred to a nitrogen-filled glove box for $CsPbI_2Br$ perovskite deposition.

The $CsPbI_2Br$ perovskite film preparation was based on a two-step thermal annealing method, following a previously reported technique with minor modification.[8] Briefly, the precursor solution was prepared by stirring 277 mg PbI_2, 220-mg $PbBr_2$, and 312 mg CsI in 1-mL DMSO at 80 °C until completely dissolved. It was then filtered using a PTFE membrane with a 0.2-µm pore size before usage. The $CsPbI_2Br$ precursor (70 µL) was dropped onto the ZnO film and spin-coated at a speed of 1500 rpm for 10 s as the first step and then at 2500 rpm for 50 s as the second step. The annealing process was performed using the two-step method, at 41 °C for 4 min as the first step. It was then directly placed on a 160 °C hotplate for 10 min. After the substrate was cooled to room temperature, the P3HT solution (10 mg/mL in chlorobenzene) was spin-coated on top of perovskite at 3500 rpm for 30 s. Finally, MoO_x and Ag were deposited using thermal evaporation with a thickness of 15 and 100 nm, respectively.

For the organic BHJ single-junction device, the photoactive solution was prepared by stirring PTB7-Th and IEICO-4F (1:1.5 weight ratio) in chlorobenzene:1-chloronaphthalene (tech 85%, Alfa Aesar) (96:4 volume ratio) solvent mixture with a concentration of 25 mg/mL. The stirring process was performed at 100 °C for 2 h. The organic BHJ solution was filtered before utilization. The spin coating process of the organic BHJ solution was executed at 1500 rpm for 120 s to yield a film thickness of 125 nm. To complete the device, MoO_x and Ag were thermally evaporated with 7- and 100-nm thicknesses, respectively.

14

Hybrid tandem device fabrication: The CsPbI$_2$Br front cell was prepared using a similar method in a single-junction device with a thin layer of Au (1 nm) deposited on the MoO$_x$ layer instead of Ag. The Au deposition rate was maintained at 0.1 Å/s, and the sample holder was rotated to ensure homogeneous coverage of Au. The ZnO nanoparticles solution in the mixed solvents of ethanol and isopropanol was spin-coated at 6000 rpm for 30 s, followed by drying for a few min. The organic BHJ layer was prepared using a similar procedure in a single-junction device. Finally, the MoO$_x$ and Ag were deposited under reduced pressure (10^{-7} Torr) with 7- and 100-nm thicknesses, respectively, to complete the tandem device.

Characterizations: The *J–V* characteristic of the devices was obtained using a Keithley 2401 instrument under simulated AM 1.5G sunlight in a nitrogen-filled glovebox. The certified monosilicon standard cell was used to calibrate the light intensity. The active area of the device was determined by a black shadow mask with a 5.18-mm^2 area.[60] The EQE measurement of the tandem device was performed using QUANTX-300 and by referring to the reported procedure.[50] The light source (quartz tungsten halogen lamp, 150 W) was filtered using short pass (10SWF-500-B) and long pass (10LWF-850-B) edge filters for front- and back-cell light bias illumination, respectively. To minimize the overestimation in each sub-cell EQE, a forward electrical bias was applied during the measurement. This effect can appear because of the increment of the electric field effect from optical bias illumination.[50] A monochromatic light with 100 Hz frequency was used in the EQE measurement, and its intensity was calibrated with a Si/Ge photodiode reference (Newport). Cross-sectional images of the devices were acquired from a field-emission SEM (JEOL JSM-7610F).

Optical simulation: The TMF method was used to perform optical simulation in the tandem device. The MATLAB code for this simulation was obtained from the McGehee Group.[61] The optical

constants of the $CsPbI_2Br$ and organic BHJ films were measured using ellipsometry spectroscopy (VASE, J.A. Woollam Co. Inc.), whereas the optical constants of other films was determined from our previously reported values.[32]

Semi-empirical model analysis: Semi-empirical modeling on a monolithic two-junction tandem photovoltaic device in series connection employed a similar reported method with a slight modification in the fundamental assumption.[25] Briefly, the achievable PCEs were obtained following the equation PCE = $J_{SC} \times V_{OC} \times FF/P_{in}$, where J_{SC} is the short-circuit current density, V_{OC} is the open-circuit voltage, FF is the fill factor, and P_{in} is the input power density of the incident light. The J_{SC} value of each sub-cell was obtained by integrating the estimated external quantum efficiency (EQE) with the incident photon in the entire absorption range, whereas the J_{SC} of the tandem device was determined by the lower J_{SC} value of either of the two sub-cells. The V_{OC} of the tandem device was assumed to be the sum of V_{OC} at each sub-cell. The V_{OC} of each sub-cell was obtained by the equation $eV_{OC} = E_g - E_{loss}$, where e is the elementary charge, E_g is the optical bandgap of active layers, and E_{loss} is the energy loss. The FF of the tandem device was presumed from the value in the reported state-of-the-art solution-processed tandem device.[25, 26] The assumptions we used are as follows:

1) The parasitic absorbance in the tandem device was assumed to be zero. Therefore, those layers other than photoactive materials were adjusted to be fully transparent ideally.

2) The 100% absorbance of each photoactive material was used. Thus, all photons with energies higher than the bandgap of the front cell were fully absorbed by the front cell, yielding no overlap absorption between the two sub-cells. This condition also resulted in an EQE value identical to that of IQE.

3) The given EQE was set to the same value for the entire absorption range of the active material.

4) The ideal series connection between the two sub-cells was used. Then, the V_{OC} of the tandem device was the sum of V_{OC} in each sub-cell.

The *FF* of the tandem device was assumed to be 0.78, which was comparable to the state-of-the-art value.[25]

Supporting Information
Supporting Information is available from the Wiley Online Library or from the author.

Received: ((will   be   filled   in   by   the   editorial   staff))
Revised: ((will   be   filled   in   by   the   editorial   staff))
Published online: ((will be filled in by the editorial staff))

References

1   H. Wei, Y. Fang, P. Mulligan, W. Chuirazzi, H.-H. Fang, C. Wang, B. R. Ecker, Y. Gao, M. A. Loi, L. Cao and J. Huang, *Nature Photonics*, 2016, **10**, 333.
2   Z. Chen, Q. Dong, Y. Liu, C. Bao, Y. Fang, Y. Lin, S. Tang, Q. Wang, X. Xiao, Y. Bai, Y. Deng and J. Huang, *Nature Communications*, 2017, **8**, 1890.
3   S. D. Stranks, G. E. Eperon, G. Grancini, C. Menelaou, M. J. P. Alcocer, T. Leijtens, L. M. Herz, A. Petrozza and H. J. Snaith, *Science*, 2013, **342**, 341.
4   D. Shi, V. Adinolfi, R. Comin, M. Yuan, E. Alarousu, A. Buin, Y. Chen, S. Hoogland, A. Rothenberger, K. Katsiev, Y. Losovyj, X. Zhang, P. A. Dowben, O. F. Mohammed, E. H. Sargent and O. M. Bakr, *Science*, 2015, **347**, 519.
5   NREL, Best Research-Cell Efficiencies, https://www.nrel.gov/pv/assets/pdfs/pv-efficiency-chart.20190103.pdf).
6   S. Wang, Y. Jiang, Emilio J. Juarez-Perez, Luis K. Ono and Y. Qi, *Nature Energy*, 2016, **2**, 16195.
7   J. S. Manser, M. I. Saidaminov, J. A. Christians, O. M. Bakr and P. V. Kamat, *Accounts of Chemical Research*, 2016, **49**, 330-338.
8   C. Liu, W. Li, C. Zhang, Y. Ma, J. Fan and Y. Mai, *Journal of the American Chemical Society*, 2018, **140**, 3825-3828.

9   W. Chen, H. Chen, G. Xu, R. Xue, S. Wang, Y. Li and Y. Li, *Joule*, 2019, **3**, 191-204.

10   S. Mariotti, O. S. Hutter, L. J. Phillips, P. J. Yates, B. Kundu and K. Durose, *ACS Applied Materials & Interfaces*, 2018, **10**, 3750-3760.

11   J. Duan, Y. Zhao, B. He and Q. Tang, *Angewandte Chemie International Edition*, 2018, **57**, 3787-3791.

12   K. C. Tang, P. You and F. Yan, *Solar RRL*, 2018, **2**, 1800075.

13   G. E. Eperon, G. M. Paternò, R. J. Sutton, A. Zampetti, A. A. Haghighirad, F. Cacialli and H. J. Snaith, *Journal of Materials Chemistry A*, 2015, **3**, 19688-19695.

14   Y. Wang, M. I. Dar, L. K. Ono, T. Zhang, M. Kan, Y. Li, L. Zhang, X. Wang, Y. Yang, X. Gao, Y. Qi, M. Grätzel and Y. Zhao, *Science*, 2019, **365**, 591-595.

15   Y. Zhang, C. Wu, D. Wang, Z. Zhang, X. Qi, N. Zhu, G. Liu, X. Li, H. Hu, Z. Chen, L. Xiao and B. Qu, *Solar RRL*, 2019, **0**, 1900254.

16   R. J. Sutton, G. E. Eperon, L. Miranda, E. S. Parrott, B. A. Kamino, J. B. Patel, M. T. Hörantner, M. B. Johnston, A. A. Haghighirad, D. T. Moore and H. J. Snaith, *Advanced Energy Materials*, 2016, **6**, 1502458.

17   L. Fu, Y. Zhang, B. Chang, B. Li, S. Zhou, L. Zhang and L. Yin, *Journal of Materials Chemistry A*, 2018, **6**, 13263-13270.

18   H. Wang, H. Bian, Z. Jin, L. Liang, D. Bai, Q. Wang and S. F. Liu, *Solar RRL*, 2018, **2**, 1800216.

19   A. D. Vos, *Journal of Physics D: Applied Physics*, 1980, **13**, 839-846.

20   Q. Tai, K.-C. Tang and F. Yan, *Energy & Environmental Science*, 2019, **12**, 2375-2405.

21   H. Yao, Y. Cui, R. Yu, B. Gao, H. Zhang and J. Hou, *Angewandte Chemie International Edition*, 2017, **56**, 3045-3049.

22   C.-C. Chen, S.-H. Bae, W.-H. Chang, Z. Hong, G. Li, Q. Chen, H. Zhou and Y. Yang, *Materials Horizons*, 2015, **2**, 203-211.

23   Q. Zeng, L. Liu, Z. Xiao, F. Liu, Y. Hua, Y. Yuan and L. Ding, *Science Bulletin*, 2019, **64**, 885-887.

24   X. Song, N. Gasparini, L. Ye, H. Yao, J. Hou, H. Ade and D. Baran, *ACS Energy Letters*, 2018, **3**, 669-676.

25   L. Meng, Y. Zhang, X. Wan, C. Li, X. Zhang, Y. Wang, X. Ke, Z. Xiao, L. Ding, R. Xia, H.-L. Yip, Y. Cao and Y. Chen, *Science*, 2018, **361**, 1094.

26   D. Zhao, C. Chen, C. Wang, M. M. Junda, Z. Song, C. R. Grice, Y. Yu, C. Li, B. Subedi, N. J. Podraza, X. Zhao, G. Fang, R.-G. Xiong, K. Zhu and Y. Yan, *Nature Energy*, 2018, **3**, 1093-1100.

27   F. Sahli, J. Werner, B. A. Kamino, M. Bräuninger, R. Monnard, B. Paviet-Salomon, L. Barraud, L. Ding, J. J. Diaz Leon, D. Sacchetto, G. Cattaneo, M. Despeisse, M. Boccard, S. Nicolay, Q. Jeangros, B. Niesen and C. Ballif, *Nature Materials*, 2018, **17**, 820-826.

28   M. Law, M. C. Beard, S. Choi, J. M. Luther, M. C. Hanna and A. J. Nozik, *Nano Letters*, 2008, **8**, 3904-3910.

29   A. Armin, M. Velusamy, P. Wolfer, Y. Zhang, P. L. Burn, P. Meredith and A. Pivrikas, *ACS Photonics*, 2014, **1**, 173-181.

30   M. Li, K. Gao, X. Wan, Q. Zhang, B. Kan, R. Xia, F. Liu, X. Yang, H. Feng, W. Ni, Y. Wang, J. Peng, H. Zhang, Z. Liang, H.-L. Yip, X. Peng, Y. Cao and Y. Chen, *Nature Photonics*, 2016, **11**, 85.

31   J. Liu, S. Lu, L. Zhu, X. Li and W. C. H. Choy, *Nanoscale*, 2016, **8**, 3638-3646.

32   H. Aqoma, R. Azmi, S.-H. Oh and S.-Y. Jang, *Nano Energy*, 2017, **31**, 403-409.

33   L. Zuo, X. Shi, S. B. Jo, Y. Liu, F. Lin and A. K. Y. Jen, *Advanced Materials*, 2018, **30**, 1706816.

34   G. Nogay, F. Sahli, J. Werner, R. Monnard, M. Boccard, M. Despeisse, F. J. Haug, Q. Jeangros, A. Ingenito and C. Ballif, *ACS Energy Letters*, 2019, **4**, 844-845.

35   C. O. Ramírez Quiroz, G. D. Spyropoulos, M. Salvador, L. M. Roch, M. Berlinghof, J. Darío Perea, K. Forberich, L.-I. Dion-Bertrand, N. J. Schrenker, A. Classen, N. Gasparini, G. Chistiakova, M. Mews, L. Korte, B. Rech, N. Li, F. Hauke, E. Spiecker, T. Ameri, S. Albrecht, G. Abellán, S. León, T. Unruh, A. Hirsch, A. Aspuru-Guzik and C. J. Brabec, *Advanced Functional Materials*, 2019, **29**, 1901476.

36   T. Leijtens, R. Prasanna, K. A. Bush, G. E. Eperon, J. A. Raiford, A. Gold-Parker, E. J. Wolf, S. A. Swifter, C. C. Boyd, H.-P. Wang, M. F. Toney, S. F. Bent and M. D. McGehee, *Sustainable Energy & Fuels*, 2018, **2**, 2450-2459.

37   A. Rajagopal, Z. Yang, S. B. Jo, I. L. Braly, P.-W. Liang, H. W. Hillhouse and A. K. Y. Jen, *Advanced Materials*, 2017, **29**, 1702140.

38   R. Lin, K. Xiao, Z. Qin, Q. Han, C. Zhang, M. Wei, M. I. Saidaminov, Y. Gao, J. Xu, M. Xiao, A. Li, J. Zhu, E. H. Sargent and H. Tan, *Nature Energy*, 2019, **4**, 864-873.

39   J. Tong, Z. Song, D. H. Kim, X. Chen, C. Chen, A. F. Palmstrom, P. F. Ndione, M. O. Reese, S. P. Dunfield, O. G. Reid, J. Liu, F. Zhang, S. P. Harvey, Z. Li, S. T. Christensen, G. Teeter, D. Zhao, M. M. Al-Jassim, M. F. A. M. van Hest, M. C. Beard, S. E. Shaheen, J. J. Berry, Y. Yan and K. Zhu, *Science*, 2019, **364**, 475.

40   A. F. Palmstrom, G. E. Eperon, T. Leijtens, R. Prasanna, S. N. Habisreutinger, W. Nemeth, E. A. Gaulding, S. P. Dunfield, M. Reese, S. Nanayakkara, T. Moot, J. Werner, J. Liu, B. To, S. T. Christensen, M. D. McGehee, M. F. A. M. van Hest, J. M. Luther, J. J. Berry and D. T. Moore, *Joule*, 2019, **3**, 2193-2204.

41   D. P. McMeekin, S. Mahesh, N. K. Noel, M. T. Klug, J. Lim, J. H. Warby, J. M. Ball, L. M. Herz, M. B. Johnston and H. J. Snaith, *Joule*, 2019, **3**, 387-401.

42   J. Seo, Y. Moon, S. Lee, C. Lee, D. Kim, H. Kim and Y. Kim, *Nanoscale Horizons*, 2019, **4**, 1221-1226.

43   L. Meng, Y.-Q.-Q. Yi, X. Wan, Y. Zhang, X. Ke, B. Kan, Y. Wang, R. Xia, H.-L. Yip, C. Li and Y. Chen, *Advanced Materials*, 2019, **31**, 1804723.

44   G. Liu, J. Jia, K. Zhang, X. e. Jia, Q. Yin, W. Zhong, L. Li, F. Huang and Y. Cao, *Advanced Energy Materials*, 2019, **9**, 1803657.

45   P. Cheng, Y. Liu, S.-Y. Chang, T. Li, P. Sun, R. Wang, H.-W. Cheng, T. Huang, L. Meng, S. Nuryyeva, C. Zhu, K.-H. Wei, B. Sun, X. Zhan and Y. Yang, *Joule*, 2019, **3**, 432-442.

46   N. Li and C. J. Brabec, *Energy & Environmental Science*, 2015, **8**, 2902-2909.

47   Y. Li, J.-D. Lin, X. Liu, Y. Qu, F.-P. Wu, F. Liu, Z.-Q. Jiang and S. R. Forrest, *Advanced Materials*, 2018, **30**, 1804416.

48   W. Li, A. Furlan, K. H. Hendriks, M. M. Wienk and R. A. J. Janssen, *Journal of the American Chemical Society*, 2013, **135**, 5529-5532.

49   Y. Cui, H. Yao, B. Gao, Y. Qin, S. Zhang, B. Yang, C. He, B. Xu and J. Hou, *Journal of the American Chemical Society*, 2017, **139**, 7302-7309.

50   J. Gilot, M. M. Wienk and R. A. J. Janssen, *Advanced Functional Materials*, 2010, **20**, 3904-3911.

51   A. Wadsworth, M. Moser, A. Marks, M. S. Little, N. Gasparini, C. J. Brabec, D. Baran and I. McCulloch, *Chemical Society Reviews*, 2019, **48**, 1596-1625.

52   Z. Yao, X. Liao, K. Gao, F. Lin, X. Xu, X. Shi, L. Zuo, F. Liu, Y. Chen and A. K. Y. Jen, *Journal of the American Chemical Society*, 2018, **140**, 2054-2057.

53   H. Tan, F. Che, M. Wei, Y. Zhao, M. I. Saidaminov, P. Todorović, D. Broberg, G. Walters, F. Tan, T. Zhuang, B. Sun, Z. Liang, H. Yuan, E. Fron, J. Kim, Z. Yang, O. Voznyy, M. Asta and E. H. Sargent, *Nature Communications*, 2018, **9**, 3100.

54   C. Li, Z. Song, D. Zhao, C. Xiao, B. Subedi, N. Shrestha, M. M. Junda, C. Wang, C.-S. Jiang, M. Al-Jassim, R. J. Ellingson, N. J. Podraza, K. Zhu and Y. Yan, *Advanced Energy Materials*, 2019, **9**, 1803135.

55   J. Hou, O. Inganäs, R. H. Friend and F. Gao, *Nature Materials*, 2018, **17**, 119.

56   K. H. Hendriks, W. Li, M. M. Wienk and R. A. J. Janssen, *Journal of the American Chemical Society*, 2014, **136**, 12130-12136.

57   C. H. Peters, I. T. Sachs-Quintana, J. P. Kastrop, S. Beaupré, M. Leclerc and M. D. McGehee, *Advanced Energy Materials*, 2011, **1**, 491-494.

58   Q. Burlingame, X. Huang, X. Liu, C. Jeong, C. Coburn and S. R. Forrest, *Nature*, 2019, DOI: 10.1038/s41586-019-1544-1.

59   W. J. E. Beek, M. M. Wienk, M. Kemerink, X. Yang and R. A. J. Janssen, *The Journal of Physical Chemistry B*, 2005, **109**, 9505-9516.

60   R. Azmi, S.-H. Oh and S.-Y. Jang, *ACS Energy Letters*, 2016, **1**, 100-106.

61   G. F. Burkhard, E. T. Hoke and M. D. McGehee, *Advanced Materials*, 2010, **22**, 3293-3297.
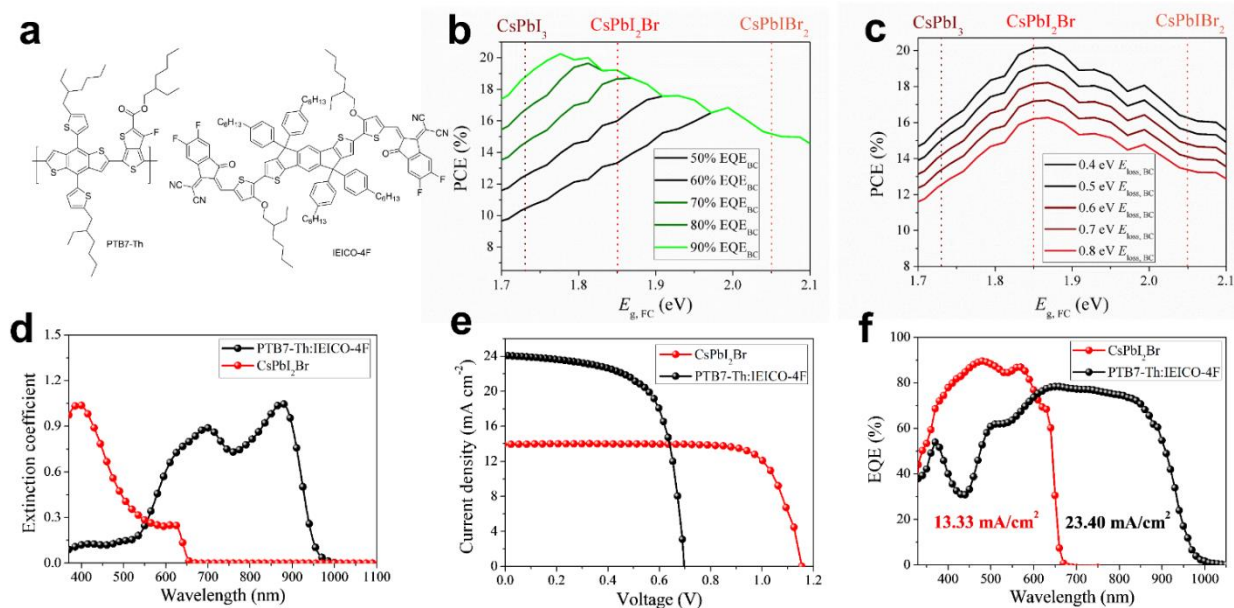
Figure 1. **a**. Chemical structure of PTB7-Th and IEICO-4F. Semi-empirical calculation results of device PCE with respect to **b**. EQE_{BC} and **c**. $E_{loss,\ BC}$. **d**. Extinction coefficient of photoactive materials. **e**. $J–V$ characteristics and **f**. EQE spectra of single-junction devices.
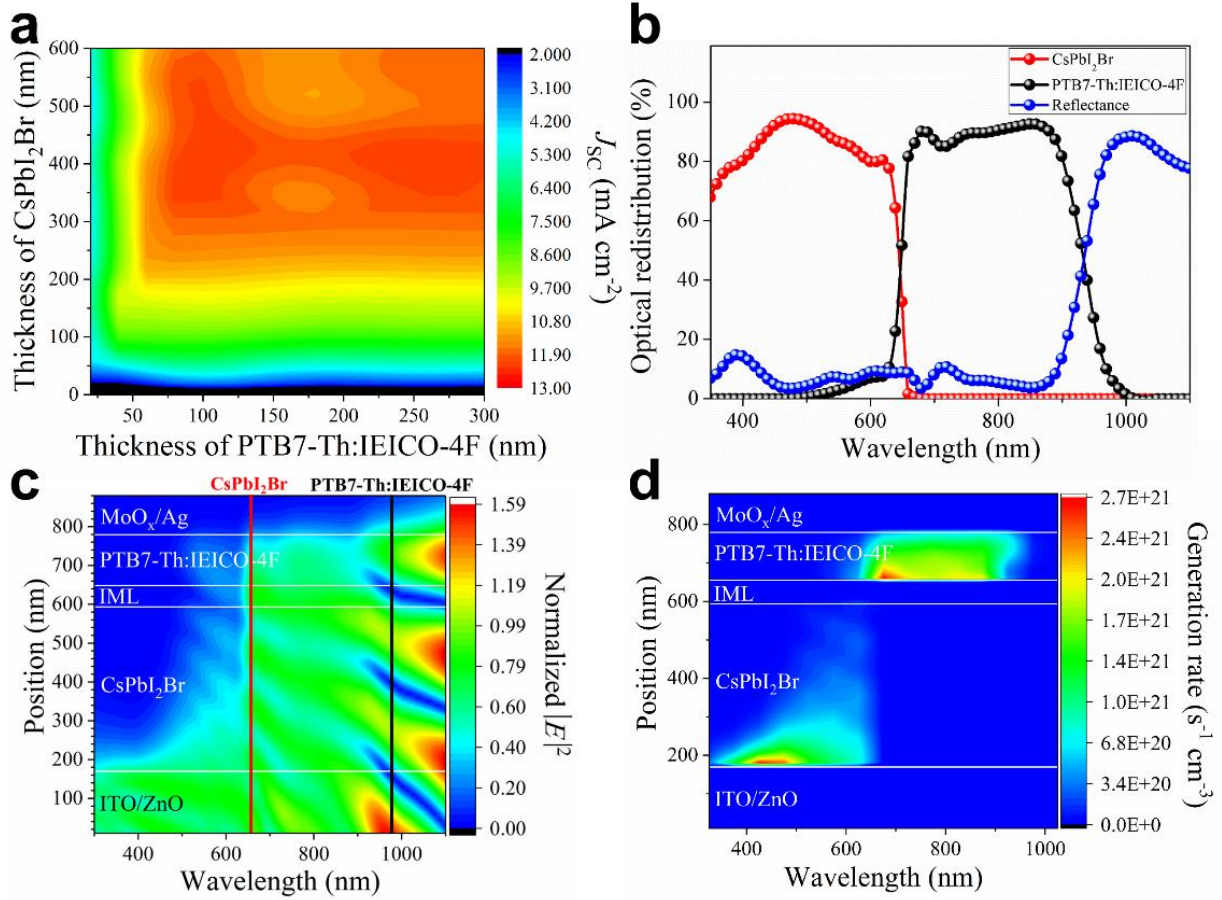
Figure 2. **a**. Simulated J_{SC} of the hybrid tandem device by TMF optical calculation with respect to the thicknesses of sub-cells. **b**. Optical redistribution of front and back cell in the hybrid tandem device. The thicknesses of the front and back cells were 400 nm and 130 nm, respectively. **c**. Normalized electric field and **d**. charge generation rate distribution spectra in the hybrid tandem device.

Table 1. Summary of single-junction and hybrid tandem device performance

Device	PCE (%)	V_{OC} (V)	J_{SC} (mA cm^{-2})	FF
CsPbI$_2$Br single	12.46 (11.84 ± 0.43)	1.15 (1.16 ± 0.037)	13.94 (13.62 ± 0.30)	0.78 (0.75 ± 0.024)
PTB7-Th:IEICO-4F single	11.02 (10.64 ± 0.30)	0.70 (0.69 ± 0.004)	24.07 (24.12 ± 0.27)	0.66 (0.64 ± 0.021)
Hybrid tandem	18.04 (17.30 ± 0.40)	1.73 (1.75 ± 0.027)	12.94 (13.07 ± 0.49)	0.81 (0.76 ± 0.020)

Figure 3. **a**. Structure of the hybrid tandem solar cell device. **b**. Cross-sectional SEM image and **c**. energy level diagram of hybrid tandem device. **d**. *J–V* characteristic of the hybrid tandem device under AM 1.5G one-sun illumination. **e**. PCE distribution of hybrid tandem devices from 50 devices. **f**. Experimental and simulated EQE of the front and back cells in the hybrid tandem device. The error bands in the simulated EQE represent a 5% thickness measurement error.
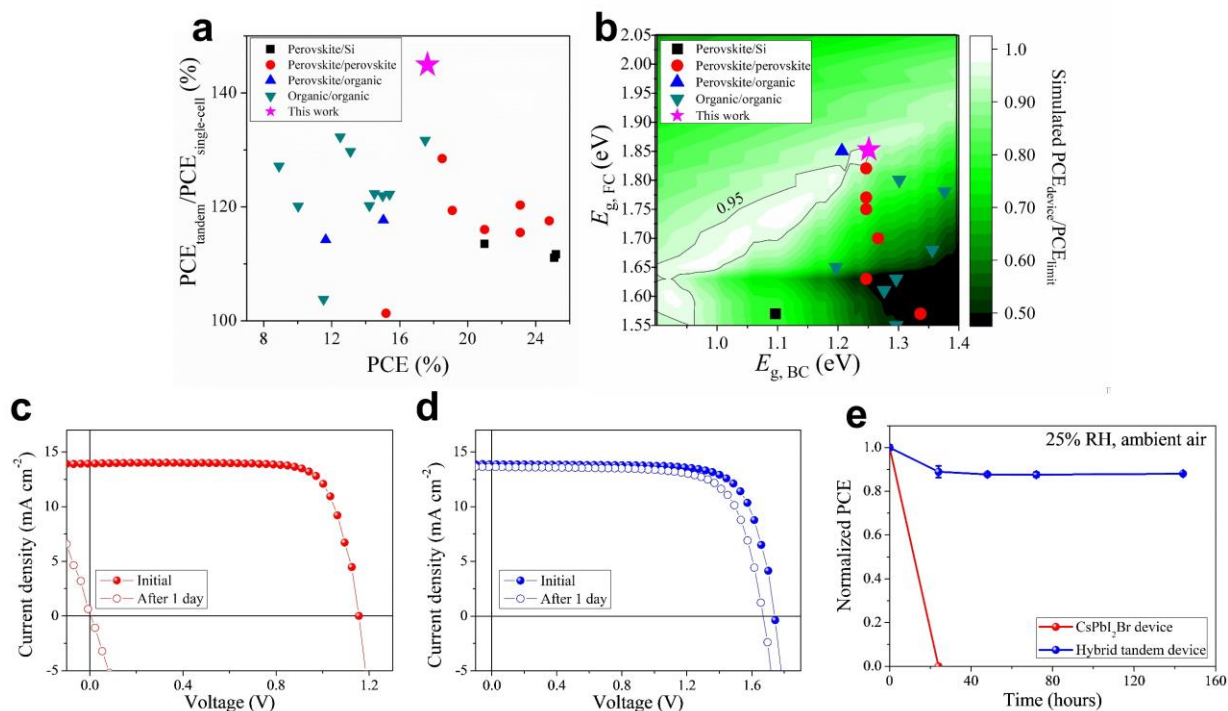
Figure 4. **a**. PCE improvement from single-junction to tandem devices in the literature. **b**. Plots of the front- and back-cell bandgaps of various tandem devices in the literature. *J-V* characteristics of the **c**. single-junction $CsPbI_2Br$ device and **d**. hybrid tandem device under ~25% relative humidity. **e**. long-term storage stability of single-junction $CsPbI_2Br$ and hybrid tandem devices in ambient air with ~25% relative humidity. All devices were tested without encapsulation.
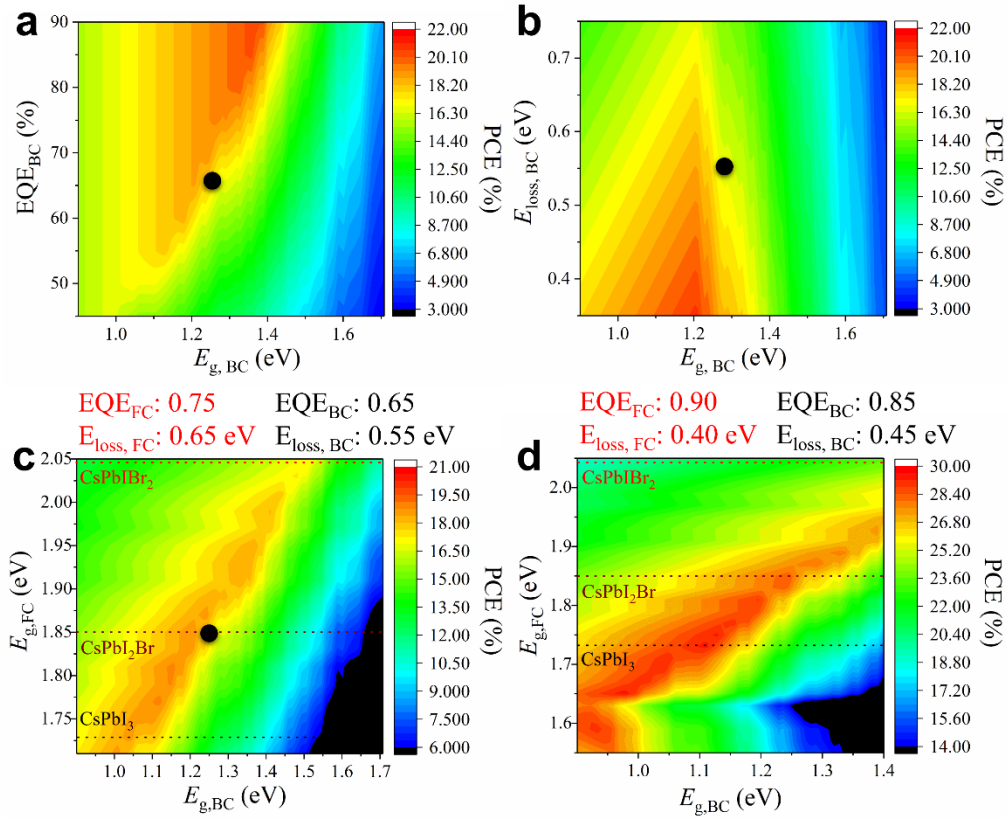
Figure 5. Semi-empirical calculation of the PCE of hybrid tandem devices with respect to **a**. EQE$_{BC}$ and $E_{g, BC}$, **b**. $E_{loss, BC}$ and $E_{g, BC}$, and **c**. $E_{g, FC}$ and $E_{g, BC}$. **d**. Semi-empirical calculation of the PCE of hybrid tandem devices with respect to $E_{g, FC}$ and $E_{g, BC}$ when using the best-reported parameters of sub-cells.

High-Efficiency Solution-Processed Two-Terminal Hybrid Tandem Solar Cells Using Spectrally Matched Inorganic and Organic Photoactive Materials are xxxxx

Keyword: xxxx

Havid Aqoma, Imil Fadli Imran, Febrian Tri Adhi Wibowo, Narra Vamsi Krishna, Wooseop Lee, Muhammad Shamim Al Mamun, Du Yeol Ryu, Sung-Yeon Jang*

High-Efficiency Solution-Processed Two-Terminal Hybrid Tandem Solar Cells Using Spectrally Matched Inorganic and Organic Photoactive Materials
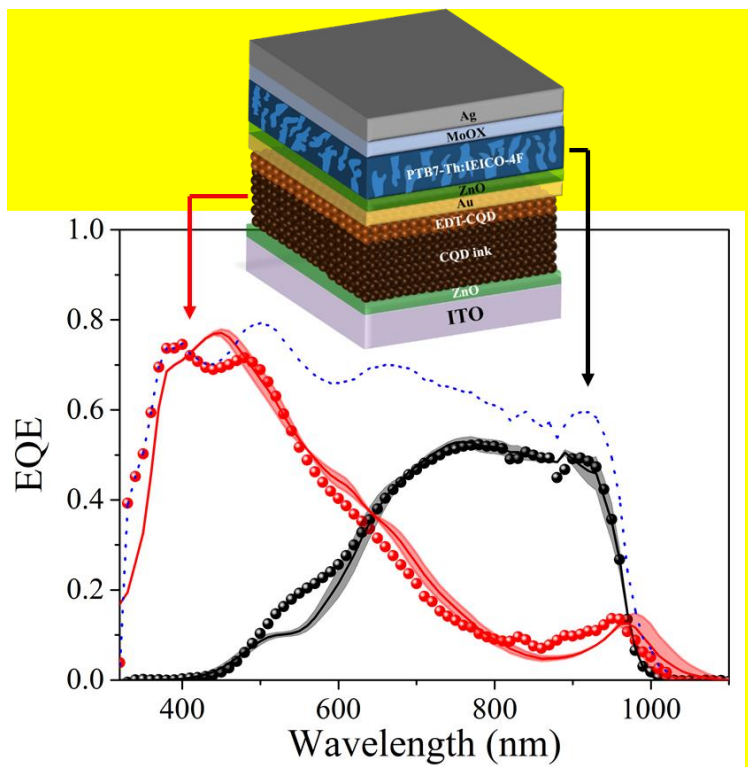
Supporting Information

High-Efficiency Solution-Processed Two-Terminal Hybrid Tandem Solar Cells Using Spectrally Matched Inorganic and Organic Photoactive Materials

Havid Aqoma, Imil Fadli Imran, Febrian Tri Adhi Wibowo, Narra Vamsi Krishna, Wooseop Lee, Muhammad Shamim Al Mamun, Du Yeol Ryu, Sung-Yeon Jang*
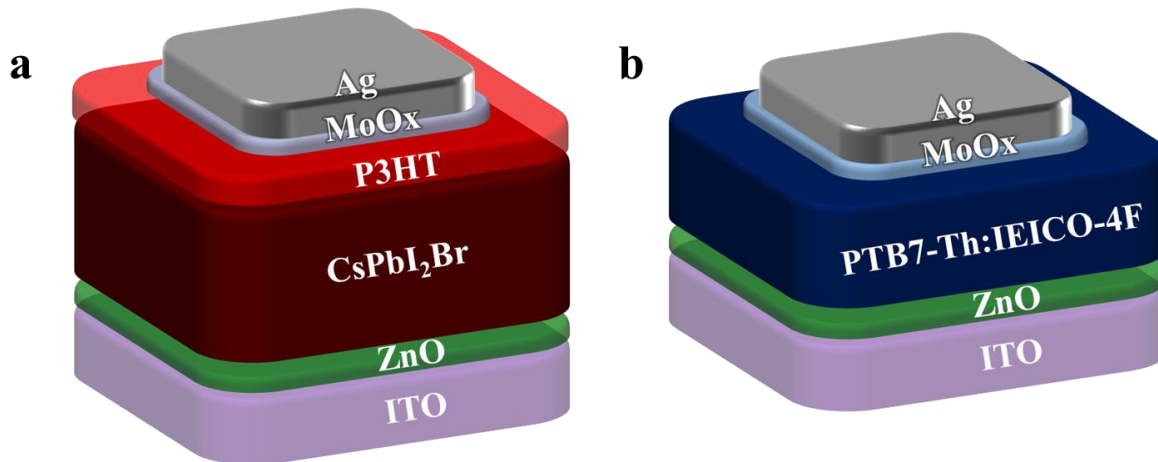
Figure S1. Structure of single-junction devices: **a**. CsPbI$_2$Br, and **b**. PTB7-Th:IEICO-4F.
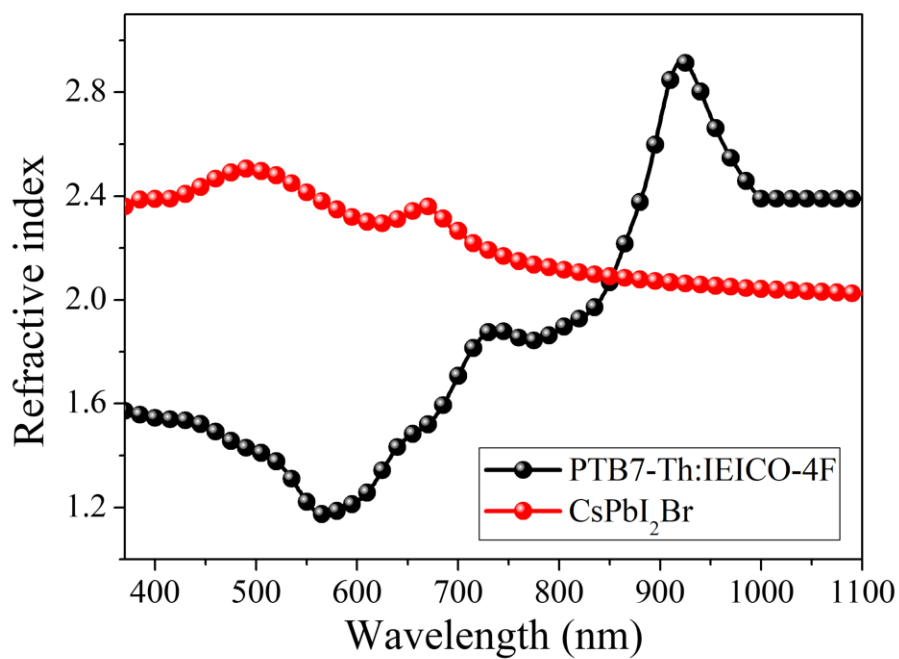
Figure S2. Refractive index (n) of CsPbI$_2$Br and PTB7-Th:IEICO-4F from variable-angle spectroscopic ellipsometry analysis.
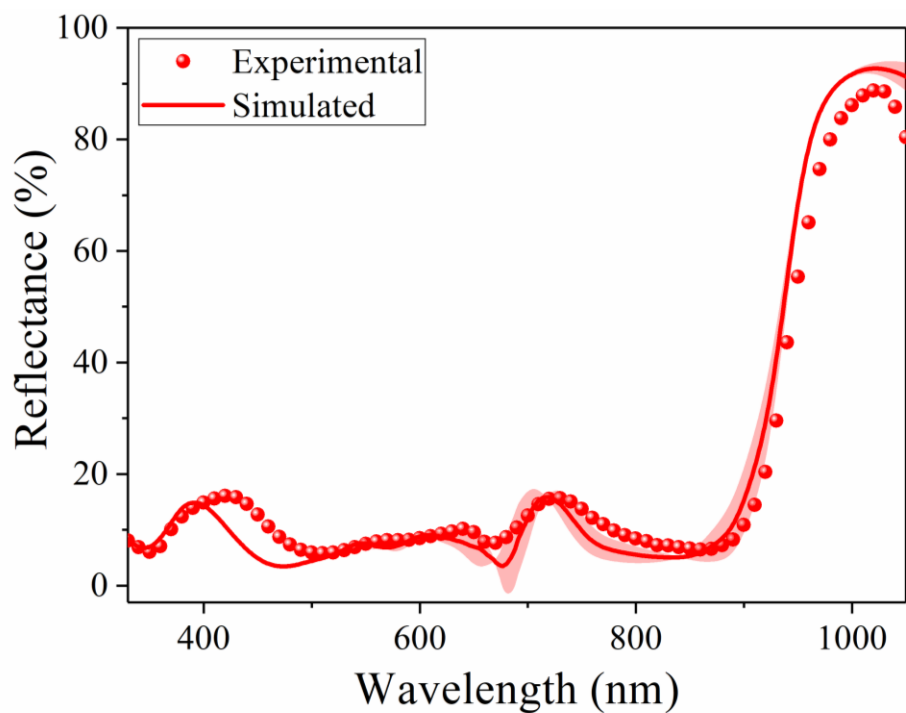
Figure S3. Comparison of simulated and experimental reflectance spectra of the hybrid tandem device. The thicknesses of the $CsPbI_2Br$ front cell and PTB7-Th:IEICO-4F back cell were 400 nm and 130 nm, respectively.
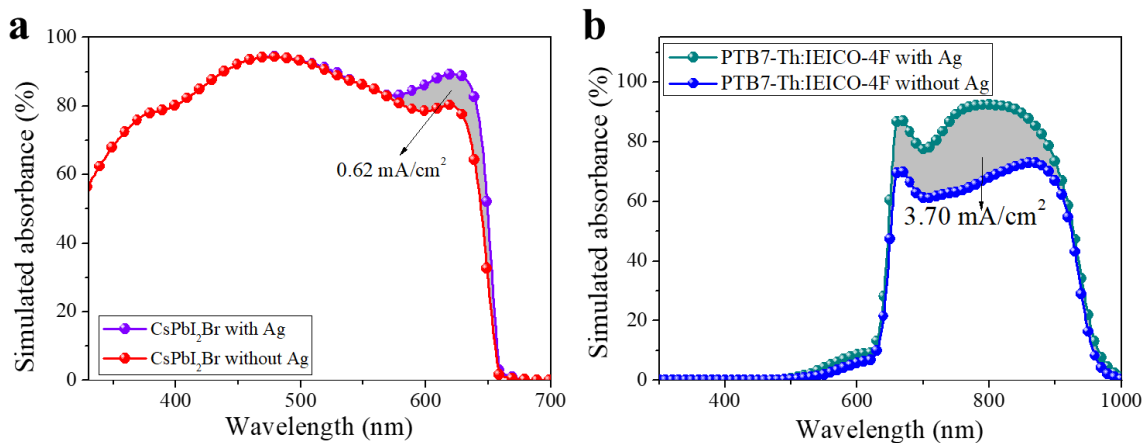
Figure S4. Simulated absorbance spectra of **a**. $CsPbI_2Br$ and **b**. PTB7-Th:IEICO-4F with and without a reflecting Ag electrode.
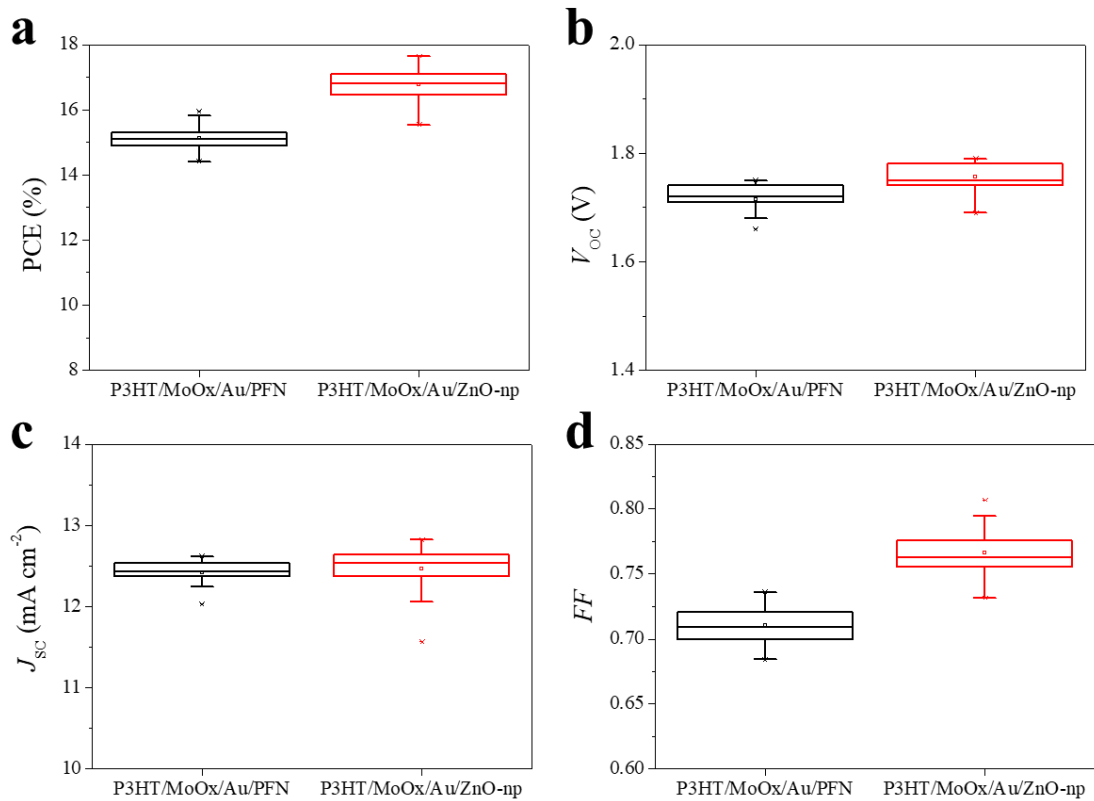
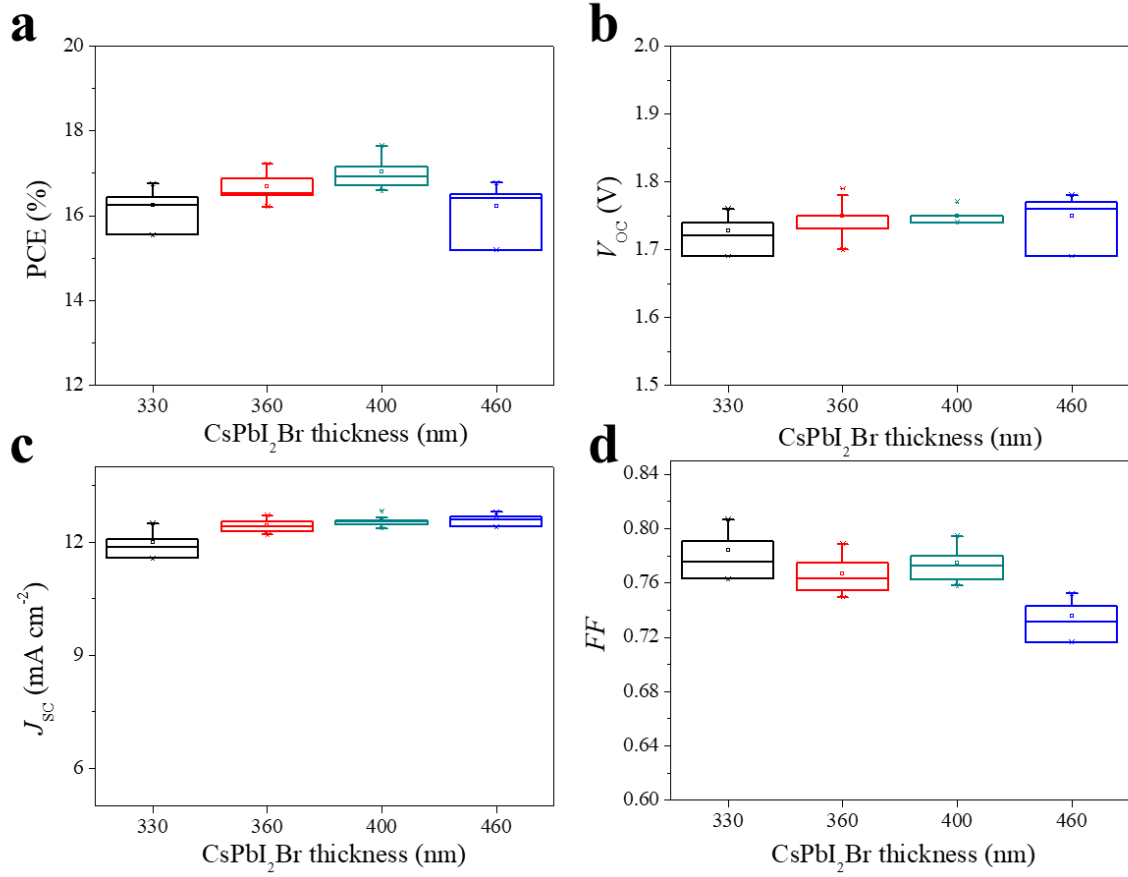Figure S5. **a**. PCE, **b**. V_{OC}, **c**. J_{SC}, and **d**. *FF* of the hybrid tandem devices using different IRLs.

Figure S6. **a**. PCE, **b**. V_{OC}, **c**. J_{SC}, and **d**. *FF* of the hybrid tandem devices with various front CsPbI₂Br layer thicknesses.
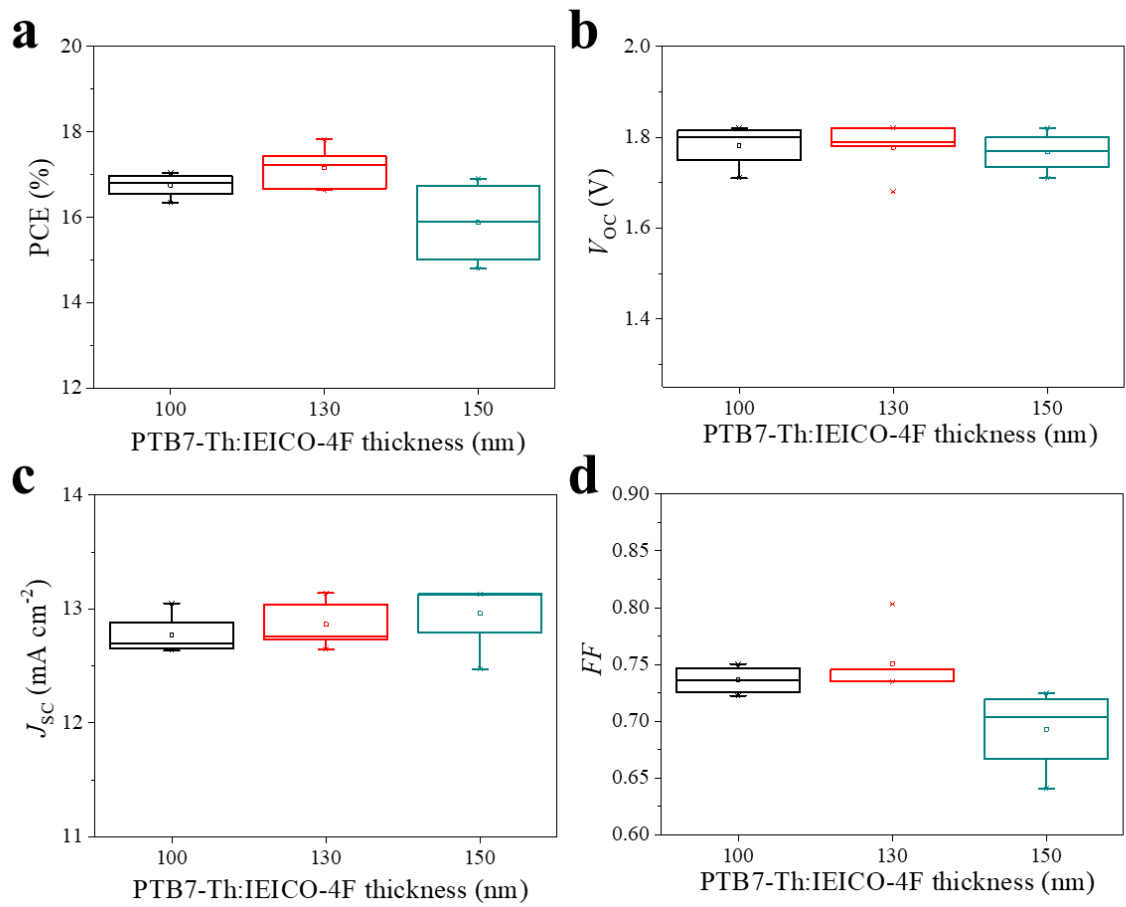
Figure S7. **a**. PCE, **b**. V_{OC}, **c**. J_{SC}, and **d**. FF of the hybrid tandem devices with various back PTB7-Th:IEICO-4F layer thicknesses.
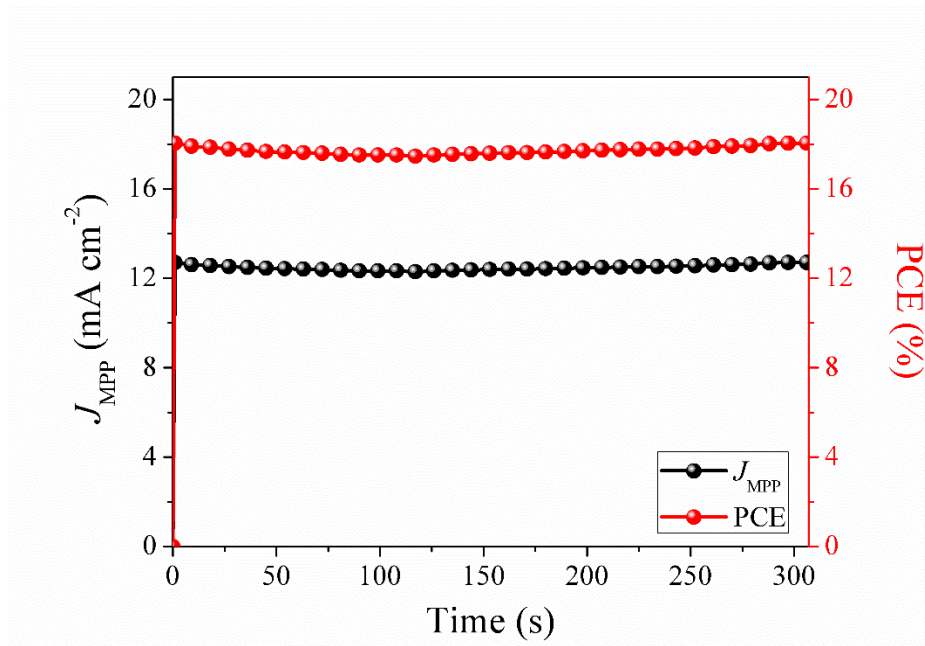
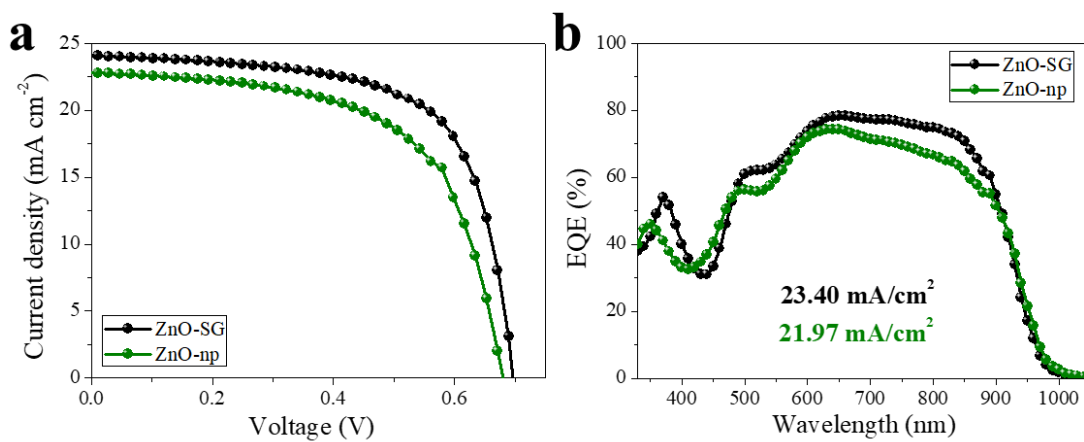Figure S8. Stabilized current output at a voltage of 1.42 V (V_{MPP}).

Figure S9. **a.** *J–V* characteristics and **b.** EQE spectra of a single-junction PTB7-Th:IEICO-4F device with two ZnO-ETLs.

Table S1. Summary of the results for the single-junction PTB7-Th:IEICO-4F device from Figure S9

Device	PCE (%)	V_{OC} (V)	J_{SC} (mA cm^{-2})	FF
ZnO-SG	11.02	0.70	24.07	0.66
	(10.64 ± 0.30)	(0.69 ± 0.004)	(24.12 ± 0.27)	(0.64 ± 0.021)
ZnO-np	9.36	0.68	22.90	0.60
	(9.03 ± 0.57)	(0.68 ± 0.006)	(22.97 ± 0.10)	(0.58 ± 0.037)